

Kinetic energy in random recurrent neural networks

Li-Ru Zhang¹ and Haiping Huang^{1,2,*}

¹*PMI Lab, School of Physics, Sun Yat-sen University, Guangzhou 510275, People's Republic of China*

²*Guangdong Provincial Key Laboratory of Magnetoelectric Physics and Devices,
Sun Yat-sen University, Guangzhou 510275, People's Republic of China*

(Dated: August 8, 2025)

The relationship between unstable fixed points and chaotic dynamics in high-dimensional neural dynamics remains elusive. In this work, we investigate the kinetic energy distribution of random recurrent neural networks by combining dynamical mean-field theory with extensive numerical simulations. We find that the average kinetic energy shifts continuously from zero to a positive value at a critical value of coupling variance (synaptic gain), with a power-law behavior close to the critical point. The steady-state activity distribution is further calculated by the theory and compared with simulations on finite-size systems. This study provides a first step toward understanding the landscape of kinetic energy, which may reflect the structure of phase space for the non-equilibrium dynamics.

INTRODUCTION

Recurrent neural networks (RNNs) with random couplings exhibit a continuous dynamical phase transition from a trivial single fixed point to non-equilibrium chaotic high-dimensional dynamics [1–3]. The dynamical phase transition shows self-organized criticality via tuning only the variance of synaptic gain despite different forms of synaptic connectivity, which offers computational advantage for reservoir computing [4–6] and toy models for better understanding population computation in real brain circuits [7–10]. However, understanding the nature of RNNs remains incomplete. A hot current debate is about whether the unstable fixed points after the chaos transition are related to the chaotic dynamics. Recent works argued that the fixed point ensemble provides transiently attractive landmarks that guide the chaotic flow [11, 12]. Moreover, fixed points and dynamics are confined to separate shells in the phase space [11, 13]. Nevertheless, other works challenged this viewpoint and argued that the high-dimensional chaos can not be inferred from these equilibria, showing theoretical evidence in a mixture model of conservative and non-conservative forces [14].

Inspired by searching for fixed points (equilibria) in RNNs [15], we formulated the fixed point distribution as an optimization problem of minimizing kinetic energy of the dynamics [3]. To explore the relationship between the equilibria and chaotic dynamics, one first should study the landscape of kinetic energy itself. This is the main focus of the paper. By applying dynamical mean-field theory (DMFT) [14, 16], we identify a continuous transition for the stationary (in the long time limit) kinetic energy and determine the scaling exponent for the critical behavior close to the transition point. The theory is corroborated by numerical simulations. Moreover, the single time probability distribution of the chaotic activity is also derived and calculated by the DMFT, supported by simulations in a finite-size system. As kinetic energy grows, this distribution gets broadened as well. We expect this theoretical result to finally lead to new insights toward the debate.

MODEL SETTING AND DMFT

We consider a recurrent neural network composed of N interacting units whose dynamics evolve according to the following equation:

$$\partial_t x_i(t) = -x_i(t) + \sum_j J_{ij} \phi(x_j), \quad (1)$$

where $x_i(t)$ denotes the synaptic current (transformed to activity through $\phi(\cdot)$) of neuron i at time t , $\phi(x)$ is a nonlinear activation function [in this work we use $\tanh(\cdot)$], and J_{ij} are synaptic weights drawn independently from a Gaussian distribution with zero mean and variance $\frac{g^2}{N}$. Here, g is also referred to as the synaptic gain, which controls the overall level of recurrent synaptic strength in the network. When g crosses a threshold of $g_c = 1$, a dynamical phase transition is triggered from a fixed point of null activity to chaos [1]. The entire system is spontaneously driven by a fragile state slightly above g_c (Fig. 1).

In the limit of a large network size ($N \rightarrow \infty$), we apply the framework of dynamical mean-field theory (DMFT) to reduce the high-dimensional system to an effective single-unit description. Under DMFT, the dynamics of a representative neuron are governed by the following stochastic differential equation:

$$\partial_t x(t) = -x(t) + \eta(t), \quad (2)$$

where $\eta(t)$ is a Gaussian random process of zero mean that encapsulates the cumulative effect of the recurrent inputs from the rest of the network. This mean-field process can also be derived by applying the cavity method in a self-consistent way [2]. In the original network, the input current to neuron i is given by $\sum_j J_{ij} \phi(x_j(t))$. Since the weights J_{ij} are drawn independently from a Gaussian distribution, independent of neural activity as well, the total input can be approximated as a Gaussian random variable due to the central limit theorem. Crucially, the effective noise $\eta(t)$ is not white, but temporally correlated. The second-order statistics are thus determined

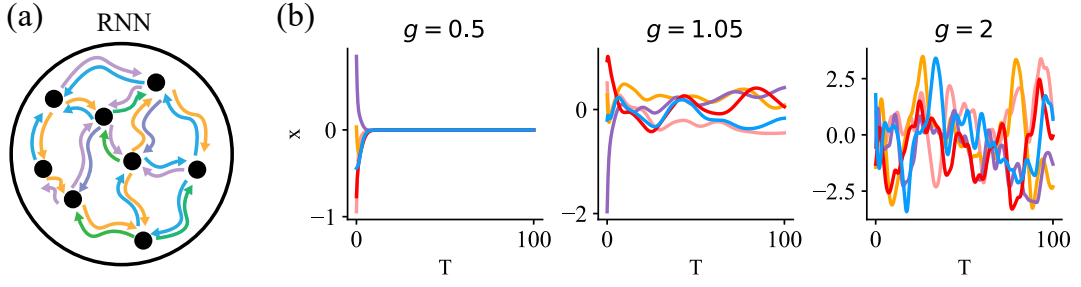


FIG. 1: Sketch of network connectivity and dynamics. (a) Schematic illustration of the RNN connectivity structure. (b) Sample trajectories of five neurons for coupling strengths $g = 0.5, 1.05, 2$.

self-consistently by the network's own dynamics:

$$\langle \eta(t)\eta(t') \rangle_\eta = g^2 C_{tt'}, \quad (3)$$

where $C_{tt'}$ is the autocorrelation function. The DMFT becomes closed and self-consistent by linking this correlation structure of the effective input noise $\eta(t)$ to the nonlinear activity of the neuron through:

$$C_{tt'} = \langle \phi(t)\phi(t') \rangle_\eta, \quad (4)$$

which means that the noise $\eta(t)$, although modeled as an external Gaussian field in the reduced mean-field description, actually emerges from the collective activity of the network itself.

To further characterize the system's dynamics, we introduce the autocorrelation function of the raw neural activity:

$$\Delta_{tt'} = \langle x(t)x(t') \rangle_\eta. \quad (5)$$

By multiplying both sides of Eq. (2) and averaging over η , one obtains the following relation:

$$(\partial_t + 1)(\partial_{t'} + 1)\Delta_{tt'} = g^2 C_{tt'}. \quad (6)$$

Assuming that the system reaches a stationary regime, we consider the time-translationally invariant (TTI) limit where both $t, t' \rightarrow \infty$, and only the time lag ($\tau = t - t'$) matters. In this regime, we can simplify the derivatives as $\partial_t = \partial_\tau$, $\partial_{t'} = -\partial_\tau$. In the TTI limit, we have the following motion equation:

$$(1 - \partial_\tau^2)\Delta_\tau = g^2 C_\tau. \quad (7)$$

We further distinguish between the equal-time and time-lagged (τ -lagged) correlations, $\Delta_\tau = \Delta$ and Δ_0 , respectively.

Since $x(t)$ is a zero-mean Gaussian process whose covariance matrix is a function of Δ and Δ_0 , the nonlinear correlation function $C_{tt'}$ can be written as [17]:

$$C(\Delta; \Delta_0) = g^2 \int Dz \left[\int Dx \phi(x\sqrt{\Delta_0 - |\Delta|} + z\sqrt{|\Delta|}) \right]^2, \quad (8)$$

where Dx and Dz denote the integration measure over standard Gaussian random variables. To provide an intuitive picture of the system's evolution, we introduce an effective potential function $V(\Delta; \Delta_0)$, such that:

$$\partial_\tau^2 \Delta = -\frac{\partial V(\Delta; \Delta_0)}{\partial \Delta}. \quad (9)$$

This leads to the explicit form by applying Price's theorem [?]:

$$V(\Delta; \Delta_0) = -\frac{\Delta^2}{2} + g^2 \int Dz \left[\int Dx \Phi \left(x\sqrt{\Delta_0 - |\Delta|} + z\sqrt{|\Delta|} \right) \right]^2. \quad (10)$$

where $\Phi(x) = \int_0^x dy \phi(y)$. A detailed derivation of the DMFT equations and the associated potential function can be found in Appendix or in Ref. [16]. In the following section, we use this theoretical framework to investigate the kinetic energy properties and probability distributions of neural activity in RNNs.

KINETIC ENERGY ANALYSIS

In this section, we present the results of our numerical simulations and theoretical predictions for the average kinetic energy in random RNNs. We also derive the scaling law of kinetic energy in the critical regime where $g \rightarrow 1^+$. Furthermore, we examine the stationary distribution of RNN activity obtained from DMFT and analyze the arc length of neural trajectories, which provides insights into the temporal evolution of the network dynamics.

Average kinetic energy

Starting from Eq. (2), multiplying both sides and taking the long-time limit, we obtain:

$$\begin{aligned}\Gamma_{tt'} &\equiv \langle \partial_t x(t) \partial_{t'} x(t') \rangle \\ &= \int \frac{d\omega}{2\pi} \int \frac{d\omega'}{2\pi} \omega \omega' \langle \hat{x}(\omega) \hat{x}^*(\omega') \rangle e^{-i\omega t} e^{i\omega' t'} \\ &\stackrel{\text{TTI}}{=} \int \frac{d\omega}{2\pi} \int \frac{d\omega'}{2\pi} \omega^2 2\pi \delta(\omega - \omega') \hat{\Delta}(\omega) e^{-i\omega t} e^{i\omega' t'} \quad (11) \\ &= \int \frac{d\omega}{2\pi} \omega^2 \hat{\Delta}(\omega) e^{-i\omega \tau} \\ &= -\partial_\tau^2 \Delta_\tau,\end{aligned}$$

where the Fourier transformation is applied (Technical details can be found in Appendix). According to Eq. (7), which relates $\partial_\tau^2 \Delta_\tau$ to C_τ , the average kinetic energy ($\frac{1}{2} \mathbf{v}^2$, where \mathbf{v} is the velocity) can be written as $\Gamma(\Delta; \Delta_0)$ in the TTI limit of $\Gamma_{tt'}$:

$$\Gamma(\Delta; \Delta_0) = \frac{\partial V(\Delta; \Delta_0)}{\partial \Delta} = g^2 C(\Delta; \Delta_0) - \Delta. \quad (12)$$

Taking the limit $\tau \rightarrow 0$, we obtain the average kinetic energy at equal times:

$$\Gamma(\Delta_0) = g^2 C(\Delta_0) - \Delta_0 = g^2 \int Dz \left[\phi(z\sqrt{|\Delta_0|}) \right]^2 - \Delta_0. \quad (13)$$

In the long-time limit, the velocity at distant time separation becomes uncorrelated:

$$\lim_{\tau \rightarrow \infty} \Gamma(\tau) = 0. \quad (14)$$

To compute the average kinetic energy (the prefactor 1/2 is neglected for convenience), one should first determine the value of Δ_0 . To accomplish this, we should notice that thanks to the motion equation [Eq. (9)], the energy is conserved at the initial and final state, i.e., $V(0; \Delta_0) = V(\Delta_0; \Delta_0)$. Therefore, we solve the following energy-conservation equation $\mathcal{F}(\Delta; \Delta_0)$ evaluated at $\Delta = \Delta_0$, corresponding to the energy conservation:

$$\begin{aligned}\mathcal{F}(\Delta; \Delta_0) &= -\frac{\Delta^2}{2} + g^2 \int Dz \left[\int Dx \Phi \left(x\sqrt{\Delta_0 - |\Delta|} + z\sqrt{|\Delta|} \right) \right]^2 \\ &\quad - g^2 \left[\int Dz \Phi \left(\sqrt{\Delta_0} z \right) \right]^2,\end{aligned} \quad (15)$$

which allows us to compute the DMFT prediction for the average kinetic energy. We use a Python-based numerical solver to find the solution of $\mathcal{F}(\Delta_0; \Delta_0) = 0$, and then substitute the resulting Δ_0 back into Eq. (13). During the numerical procedure, we set a convergence threshold of 10^{-10} , and ensure that each solution satisfies $\mathcal{F}(\Delta_0; \Delta_0) < 10^{-5}$. We repeat the root-finding process 100 times and compute the average value

of $\Gamma(\Delta_0)$ (denoted as Γ_0 below), with the standard deviation shown as an error bar in the plot.

Figure 2 compares the average kinetic energy obtained from direct simulation of Eq. (1) with the DMFT prediction from Eq. (13). The left panel shows results for a wide range of coupling strengths $0.8 \leq g \leq 1.5$, while the right panel zooms in the near-critical region $0.9 \leq g \leq 1.2$. We observe excellent agreement between the simulation results and the DMFT theory. Moreover, the fluctuations in the simulated data decrease as the network size increases, as expected.

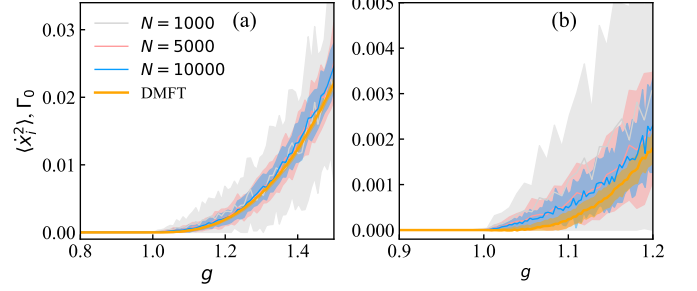


FIG. 2: The average kinetic energy of the system versus synaptic gain g . (a) Results for $0.8 \leq g \leq 1.5$; (b) An enlarged view of the critical regime $0.9 \leq g \leq 1.2$. Simulations were performed using networks of size $N = 1000, 5000$, and 10000 , with error bars computed from 100 independent realizations. The DMFT result is obtained by numerically solving $\mathcal{F}(\Delta_0; \Delta_0) = 0$ for Δ_0 , and substituting the solution into Eq. (13). Error bars for the DMFT prediction are computed from 100 numerical evaluations.

Critical behavior of kinetic energy at $g \rightarrow 1^+$

In the critical limit $g \rightarrow 1^+$, the equal-time correlation Δ_0 tends to zero. Because Δ is bounded by Δ_0 [17], $|\Delta| \ll 1$ holds for all τ as $\sigma = g - 1 \rightarrow 0^+$. In this regime, we expand both the potential function $V(\Delta; \Delta_0)$ and the energy-conservation function $\mathcal{F}(\Delta; \Delta_0)$ in powers of Δ and Δ_0 , and retain terms up to the leading nontrivial (fourth) order:

$$\begin{aligned}V(\Delta; \Delta_0) &\sim g^2 \left(\frac{1}{4} \Delta_0^2 - \frac{1}{4} \Delta_0^3 + \frac{1}{16} \Delta_0^4 \right) \\ &\quad + [-1 + g^2(1 - 2\Delta_0 + 5\Delta_0^2)] \frac{\Delta^2}{2} + g^2 \frac{\Delta^4}{6},\end{aligned} \quad (16)$$

which separates into a constant term (independent of Δ) and a Δ -dependent part. As discussed previously, $\mathcal{F}(\Delta; \Delta_0)$ is defined as the difference between the potential evaluated at an arbitrary Δ and its value at the fixed point $\Delta = 0$. Therefore, by substituting $\Delta = \Delta_0$ into Eq. (16), we obtain the expansion of $\mathcal{F}(\Delta; \Delta_0)$:

$$\mathcal{F}(\Delta_0; \Delta_0) \sim [-1 + g^2(1 - 2\Delta_0 + 5\Delta_0^2)] \frac{\Delta_0^2}{2} + g^2 \frac{\Delta_0^4}{6}. \quad (17)$$

According to Eq. (17), we solve $\mathcal{F}(\Delta_0; \Delta_0) = 0$ for Δ_0 near the critical point $g = 1 + \sigma$, where $\sigma \rightarrow 0^+$, obtaining the following expansion:

$$\Delta_0 \sim \sigma + \frac{7}{6}\sigma^2 + \mathcal{O}(\sigma^3). \quad (18)$$

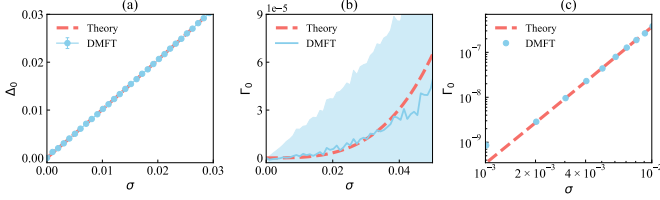


FIG. 3: Comparison between the theoretical prediction [Eq. (18) or Eq. (20)] in the limit $g \rightarrow 1^+$ and the numerical results from DMFT. (a) The dependence of Δ_0 on σ ; (b) Γ_0 obtained by substituting Δ_0 into the analytical expression [Eq. (19)]. The DMFT error bar is estimated from 100 independent numerical evaluations. (c) Enlarged view of the comparison close to the critical point in log-log scale. Note that the mean value of Δ_0 is inserted into Eq. (19).

By expanding the right-hand-side of Eq. (12) or directly taking the derivative of Eq. (16) with respect to Δ , we obtain:

$$\Gamma_0 \sim -\frac{\sigma^2}{3}\Delta_0 + (1 + 2\sigma)\frac{2\Delta_0^3}{3}. \quad (19)$$

Using Eq. (18), we derive immediately the asymptotic behavior of the kinetic energy near the critical point $g \rightarrow 1^+$:

$$\Gamma_0 \sim \frac{1}{3}\sigma^3 + \frac{59}{18}\sigma^4 + \mathcal{O}(\sigma^5). \quad (20)$$

The detailed derivation of these results is provided in Appendix . As shown in Fig. 3, the theoretical prediction of the kinetic energy in the critical regime is in excellent agreement with the numerical solution of the DMFT equations. This confirms that the scaling law of the kinetic energy near the criticality follows roughly a cubic behavior, with the theoretical scaling exponent equal to 3.

Single-time probability distribution of stationary activity

Since $x(t)$ is a Gaussian process with a fixed initial condition (chosen to be zero here), its single-time probability distribution at any time t is fully characterized by a Gaussian distribution with mean $\langle x(t) \rangle$ and variance Δ_{tt} . This distribution can be expressed as [18]:

$$P(x(t)) = \frac{1}{\sqrt{2\pi\Delta_{tt}}} \exp \left[-\frac{x - \langle x(t) \rangle}{2\Delta_{tt}} \right]. \quad (21)$$

The mean is zero, as indicated by the following formal solution:

$$x(t) = \int_{-\infty}^t ds e^{-(t-s)} \eta(s). \quad (22)$$

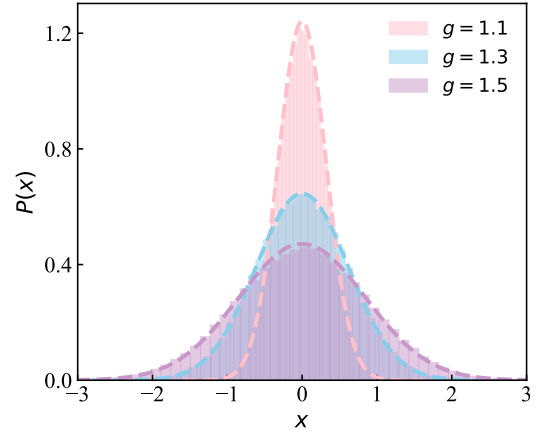


FIG. 4: Distribution of $x(t)$ at steady states for different coupling strengths of $g = 1.1, 1.3, 1.5$. Histograms represent numerical simulation results of the RNN dynamics ($N = 5000$), while dashed lines correspond to the Gaussian distributions obtained from DMFT calculations.

The variance is determined self-consistently by solving the single-unit DMFT equations [Eq. 2, see also Appendix].

To verify this theoretical prediction, we simulate RNN dynamics ($N = 5000$) and collect samples of $x(t)$ at the steady state of the system as an empirical distribution. As shown in Fig. 4, the probability density obtained from the DMFT framework (represented by the dashed lines) agrees remarkably well with the histograms derived from large-scale numerical simulations of the RNN dynamics. Furthermore, as the coupling strength g increases, the width of the distribution gets broadened, indicating a strong effect of chaotic fluctuations in the network activity. This observation is also in accord with the kinetic energy growth analyzed before.

In Fig. 5, the dynamical trajectories of the RNN and the corresponding trajectories from the DMFT equations are shown for different values of g . As g increases, the fluctuations in the trajectories become more pronounced. The algorithmic steps for solving the DMFT equation [Eq. (2)] can be found in Appendix .

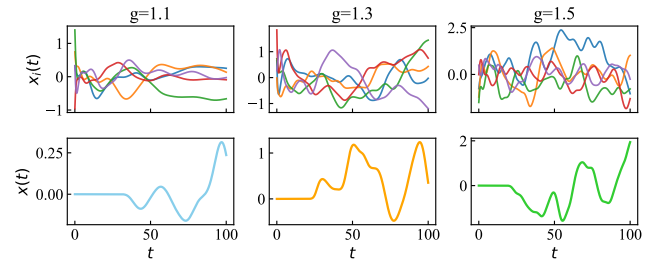


FIG. 5: Dynamical trajectories of the RNN (network size 5000) and the corresponding trajectories from the DMFT equations. Parameters from left to right: $g = 1.1, 1.3, 1.5$.

Arc Length parametrization of RNN activity

In this section, we study the arc length of RNN trajectories. As time flows, the activity travels along a curve in the manifold embedded in an ambient space of \mathbb{R}^N . The arc length is thus the cumulative distance traveled from t_0 to t , depending on an integral of speed (related to the kinetic energy). We can compare the results with predictions from DMFT. The arc length $s(t)$ from an initial time t_0 to time t is thus defined as follows:

$$s(t) = \int_{t_0}^t \sqrt{\frac{1}{N} \sum_{i=1}^N \left(\frac{dx_i(\tau)}{d\tau} \right)^2} d\tau, \quad (23)$$

where the speed is taken as a population average.

As shown in Fig. 6 (a,c), we estimate the arc length of RNNs at various coupling strengths $g = 1.2, 1.3, 1.5$, with network sizes of $N = 2000$ or $N = 5000$. Each trajectory is averaged over 100 independent realizations of RNN dynamics. The results demonstrate that, in the chaotic regime, the arc length increases with time, and this growth rate becomes larger for stronger coupling strengths. In the long-time limit, the system reaches a steady state, resulting in a rough linear growth of arc length with time.

In Fig. 6(b,d), we perform a linear fit to the arc length trajectory over the final interval $t \in [95, 100]$. The resulting slope k_s is extracted for different values of g . According to the theoretical framework presented earlier, in the steady state, this slope is expected to match the square root of the system's kinetic energy $\sqrt{\Gamma_0}$, predicted by DMFT. We thus compare the fitted slope k_s of the simulated arc length with the DMFT prediction $k_d = \sqrt{\Gamma_0}$, where Γ_0 is computed via Eq. (13) using the self-consistent solution of $\mathcal{F}(\Delta_0; \Delta_0) = 0$. As shown in Fig. 6(b,d), the error bars represent the standard deviation over 100 evaluations of Eq. (13), confirming that the arc length is directly related to the kinetic energy of the system. The agreement between the fitted slopes and DMFT predictions further validates this connection. The discrepancies between simulation and theory arise in the case of g close to g_c , probably due to numerical precision in both solving the self-consistent equation and simulating the RNN dynamics.

CONCLUSION

In this work, we study the kinetic energy level of the high-dimensional neural dynamics in the long-time limit. Supposing that the kinetic energy in the stationary limit is an order parameter, a continuous chaos transition is identified, consistent with previous studies with different order parameters [3, 16]. Furthermore, the scaling behavior of the kinetic energy is theoretically analyzed around the critical point, and a power law is identified. By solving the DMFT equations, we also calculate the single-time probability distribution of activity underlying the non-zero kinetic energy, which is in perfect agreement with experiments. One can also study the arc length

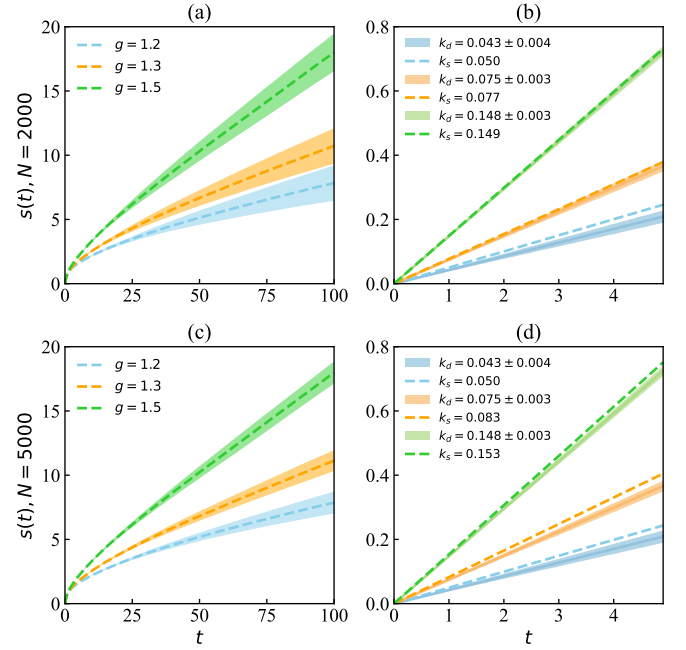


FIG. 6: Arc length of RNN trajectories and comparison with DMFT results. For simulations, two network sizes are considered. In simulations, $dt = 0.1$ being the time unit. (a, c) Arc length computed for RNNs with coupling strengths $g = 1.2, 1.3, 1.5$, averaged over 100 realizations. (b, d) The slope k_s of arc length obtained by a linear fitting over the last 50 time steps is compared with the DMFT-predicted slope $k_d = \sqrt{\Gamma_0}$ from Eq. (13). Error bars represent standard deviations across 100 trajectories. For focusing on the slope, the intercept c in the linear fit $s(t) = kt + c$ is set to zero in the plot.

traveled along the chaotic manifold, which can be further analyzed in the context of computational tasks such as perception or other types of brain states [19, 20]. In future works, it is interesting and important to determine how the dynamics are confined in the phase space to yield a given level of kinetic energy. Our recent work gave a slow-dynamics framework [13], which must be further generalized to a more challenging setting as used in this paper.

This research was supported by the National Natural Science Foundation of China for Grant numbers 12475045 and 12122515, and Guangdong Provincial Key Laboratory of Magnetoelectric Physics and Devices (No. 2022B1212010008), and Guangdong Basic and Applied Basic Research Foundation (Grant No. 2023B1515040023).

Code availability

Codes to reproduce all results are deposited in our Github [21].

Details of DMFT Derivation

A formal solution to Eq.(2) reads:

$$x(t) = \int_{-\infty}^t ds e^{-(t-s)} \eta(s). \quad (24)$$

Since $x(t)$ is a zero-mean Gaussian process determined by its covariance matrix Δ , the nonlinear correlation function $C_{tt'}$ can be written as:

$$C_{tt'} = \int \int \frac{d\mathbf{x}}{2\pi \sqrt{\det \Delta}} \exp \left[\frac{1}{2} \mathbf{x}^T \Delta^{-1} \mathbf{x} \right] \phi(x(t)) \phi(x(t')), \quad (25)$$

where we define $\mathbf{x}^T = (x(t), x(t'))$, and the covariance matrix $\Delta \in \mathbb{R}^{2 \times 2}$ is given by:

$$\Delta = \begin{bmatrix} \Delta_{tt} & \Delta_{tt'} \\ \Delta_{t't} & \Delta_{t't'} \end{bmatrix}. \quad (26)$$

By introducing a Gaussian integral representation, the correlation $C_{tt'}$ can be expressed as:

$$C_{tt'} = \int Dz \int Dx \phi(x \sqrt{\Delta_{tt} - |\Delta_{tt'}|} + z \sqrt{|\Delta_{tt'}|}) \int Dy \phi(y \sqrt{\Delta_{t't} - |\Delta_{tt'}|} + z \sqrt{|\Delta_{tt'}|}), \quad (27)$$

where $Dz = \frac{dz}{\sqrt{2\pi}} e^{-z^2/2}$. This leads to Eq. (8) in the main text.

Next, we define the effective potential:

$$V(\Delta; \Delta_0) = -\frac{1}{2} \Delta^2 + g^2 C_{\Phi}(\Delta; \Delta_0), \quad (28)$$

where the function $\Phi(x) = \int_0^x dy \phi(y)$ is introduced, and using the Price's theorem: $\frac{\partial C_{\Phi}(\Delta; \Delta_0)}{\partial \Delta} = C_{\phi}$ (the subscript indicates the non-linear function used to compute the correlation function, e.g., $\phi = \tanh$ in this paper), we get Eq. (10).

The dynamics now depend on the initial condition Δ_0 . We next find a self-consistent solution of Δ_0 . According to the energy conservation, $V(\Delta_0; \Delta_0) = V(0; \Delta_0)$ ($\Delta = 0$ due to the chaotic decorrelation), we derive:

$$-\frac{\Delta_0^2}{2} + g^2 \int Dz \Phi^2(\sqrt{\Delta_0} z) = g^2 \left(\int Dz \Phi(\sqrt{\Delta_0} z) \right)^2, \quad (29)$$

from which the value of Δ_0 can be obtained numerically. This leads to the root finding of $\mathcal{F}(\Delta_0; \Delta_0) = 0$.

Next, we provide details about deriving Eq. (11). For the Fourier transform of $x(t)$, we define:

$$\begin{aligned} x(t) &= \frac{1}{2\pi} \int d\omega \hat{x}(\omega) e^{-i\omega t}, \\ \hat{x}(\omega) &= \int dt x(t) e^{i\omega t}. \end{aligned} \quad (30)$$

Then the time derivative is given by

$$\partial_t x(t) = \int \frac{d\omega}{2\pi} (-i\omega) \hat{x}(\omega) e^{-i\omega t}. \quad (31)$$

The two-time correlation function is:

$$\begin{aligned} \langle x(t) x(t') \rangle &= \left\langle \int \int \frac{d\omega}{2\pi} \frac{d\omega'}{2\pi} \hat{x}(\omega) \hat{x}^*(\omega') e^{-i\omega t} e^{i\omega' t'} \right\rangle \\ &= \int \int \frac{d\omega}{2\pi} \frac{d\omega'}{2\pi} \langle \hat{x}(\omega) \hat{x}^*(\omega') \rangle e^{-i\omega t} e^{i\omega' t'}, \end{aligned} \quad (32)$$

where the correlation function in the frequency domain is given by

$$\begin{aligned} \langle \hat{x}(\omega) \hat{x}^*(\omega') \rangle &= \left\langle \int dt x(t) e^{i\omega t} \int dt' x(t') e^{-i\omega' t'} \right\rangle \\ &= \int dt dt' e^{i\omega t} e^{-i\omega' t'} \langle x(t) x(t') \rangle \\ &= \int dt dt' e^{i\omega t} e^{-i\omega' t'} \Delta(t, t') \\ &\stackrel{\text{TTI}}{=} \int dt' \int d\tau e^{i\omega(\tau+t')} e^{-i\omega' t'} \Delta(\tau) \\ &= \int d\tau \Delta(\tau) e^{i\omega\tau} \int dt' e^{i(\omega-\omega')t'} \\ &= 2\pi \delta(\omega - \omega') \int d\tau \Delta(\tau) e^{i\omega\tau} \\ &= 2\pi \delta(\omega - \omega') \hat{\Delta}(\omega). \end{aligned} \quad (33)$$

To derive Eq. (33), we have used TTI, under which $\Delta_{tt'} \equiv \Delta(t - t') = \Delta(\tau) \equiv \Delta_{\tau}$ with $\tau = t - t'$, and thus the double integral over time can be rewritten using the change of variables $t = \tau + t'$. In addition, we used the identity

$$\delta(\omega - \omega') = \frac{1}{2\pi} \int dt' e^{i(\omega - \omega')t'}, \quad (34)$$

which follows from the definition of the Dirac delta function in the frequency domain. Moreover, we employed the fact that $x(t)$ is real-valued, which implies that its Fourier transform satisfies the Hermitian symmetry:

$$\hat{x}(-\omega) = \hat{x}^*(\omega), \quad (35)$$

as can be seen from

$$\hat{x}(-\omega) = \int x(t) e^{-i\omega t} dt = \left(\int x(t) e^{i\omega t} dt \right)^* = \hat{x}^*(\omega). \quad (36)$$

Putting all these together, we arrive at Eq. (11).

Kinetic energy in the limit $g \rightarrow 1^+$

Before performing the expansion, we notice that the derivatives of the potential $V(\Delta; \Delta_0)$ and the dynamical energy function $\mathcal{F}(\Delta; \Delta_0)$ are the same, since the two expressions

differ only by a constant. This can be seen below.

$$\begin{aligned} \frac{\partial V(\Delta; \Delta_0)}{\partial \Delta} &= \frac{\partial \mathcal{F}(\Delta; \Delta_0)}{\partial \Delta} = \\ &= -\Delta + g^2 \int Dz \left[\int Dx \phi(x\sqrt{\Delta_0 - |\Delta|} + z\sqrt{|\Delta|}) \right]^2, \\ \text{and } \frac{\partial^n V(\Delta; \Delta_0)}{\partial \Delta^n} &= \frac{\partial^n \mathcal{F}(\Delta; \Delta_0)}{\partial \Delta^n} = -\frac{\partial^n}{\partial \Delta^n} \left(\frac{\Delta^2}{2} \right) + \\ &+ g^2 \int Dz \left[\int Dx \phi^{(n-1)}(x\sqrt{\Delta_0 - |\Delta|} + z\sqrt{|\Delta|}) \right]^2, \end{aligned} \quad (37)$$

where the second equation is written for $n \geq 1$, and $\phi^{(n)} = (d/dx)^n \phi(x)$. We choose the activation function $\phi(x) = \tanh(x)$, which is an odd function. Consequently, all odd-order derivatives of $V(\Delta; \Delta_0)$ at $\Delta = 0$ vanish:

$$\left. \frac{\partial^n V(\Delta; \Delta_0)}{\partial \Delta^n} \right|_{\Delta=0} = 0. \quad (38)$$

To have Eq. (38), we repeatedly used Price's theorem [?].

Expanding $V(\Delta; \Delta_0)$ and $\mathcal{F}(\Delta; \Delta_0)$ for small Δ , i.e., $|\Delta| \ll 1$, we obtain:

$$\begin{aligned} \mathcal{F}(\Delta; \Delta_0) &\sim \mathcal{F}(0; \Delta_0) + \mathcal{F}'(0; \Delta_0)\Delta + \mathcal{F}''(0; \Delta_0)\frac{\Delta^2}{2} + \\ &+ \mathcal{F}'''(0; \Delta_0)\frac{\Delta^3}{3!} + \mathcal{F}''''(0; \Delta_0)\frac{\Delta^4}{4!} + \mathcal{O}(\Delta^5) \\ &= \left(-1 + g^2 \left[\int Dx \phi'(x\sqrt{\Delta_0}) \right]^2 \right) \frac{\Delta^2}{2} + \\ &+ g^2 \left[\int Dx \phi'''(x\sqrt{\Delta_0}) \right]^2 \frac{\Delta^4}{4!} + \mathcal{O}(\Delta^5), \end{aligned} \quad (39)$$

where $\mathcal{F}(0; \Delta_0) = 0$, and similarly,

$$\begin{aligned} V(\Delta; \Delta_0) &\sim V(0; \Delta_0) + V'(0; \Delta_0)\Delta + V''(0; \Delta_0)\frac{\Delta^2}{2} + \\ &+ V'''(0; \Delta_0)\frac{\Delta^3}{3!} + V''''(0; \Delta_0)\frac{\Delta^4}{4!} + \mathcal{O}(\Delta^5) \\ &= g^2 \left[\int Dx \Phi(x\sqrt{\Delta_0}) \right]^2 \\ &+ \left(-1 + g^2 \left[\int Dx \phi'(x\sqrt{\Delta_0}) \right]^2 \right) \frac{\Delta^2}{2} \\ &+ g^2 \left[\int Dx \phi'''(x\sqrt{\Delta_0}) \right]^2 \frac{\Delta^4}{4!} + \mathcal{O}(\Delta^5). \end{aligned} \quad (40)$$

Next, noticing that $\Phi(x) = \ln \cosh(x)$ in our case, we expand the relevant integrals for small Δ_0 :

$$\begin{aligned} \left[\int Dx \Phi(x\sqrt{\Delta_0}) \right]^2 &\sim \left[\int Dx \left(\frac{x^2}{2} \Delta_0 - \frac{x^4}{12} \Delta_0^2 \right) \right]^2 \\ &= \left(\frac{1}{2} \Delta_0 - \frac{1}{4} \Delta_0^2 \right)^2 = \frac{1}{4} \Delta_0^2 - \frac{1}{4} \Delta_0^3 + \frac{1}{16} \Delta_0^4, \end{aligned} \quad (41)$$

where we have used $\ln \cosh(x) \sim \frac{x^2}{2} - \frac{x^4}{12}$ for a small value of x , and $\langle x^4 \rangle = 3$ for standard Gaussian random variable x . Then,

$$\begin{aligned} \left[\int Dx \phi'(x\sqrt{\Delta_0}) \right]^2 &\sim \left[\int Dx \left(1 - x^2 \Delta_0 + \frac{2}{3} x^4 \Delta_0^2 \right) \right]^2 \\ &= (1 - \Delta_0 + 2\Delta_0^2)^2 \sim 1 - 2\Delta_0 + 5\Delta_0^2 + \mathcal{O}(\Delta_0^3), \end{aligned} \quad (42)$$

and finally,

$$\begin{aligned} \left[\int Dx \phi'''(x\sqrt{\Delta_0}) \right]^2 &\sim \left[\int Dx (-2 + 8x^2 \Delta_0 - \frac{34}{3} x^4 \Delta_0^2) \right]^2 \\ &= (-2 + 8\Delta_0 - 34\Delta_0^2)^2 \sim 4 - 32\Delta_0 + \mathcal{O}(\Delta_0^2), \end{aligned} \quad (43)$$

where we have used $\tanh(x) \sim x - x^3/3$. Thus, the expansion of $\mathcal{F}(\Delta; \Delta_0)$ reads:

$$\mathcal{F}(\Delta; \Delta_0) \sim [-1 + g^2(1 - 2\Delta_0 + 5\Delta_0^2)] \frac{\Delta^2}{2} + g^2 \frac{\Delta^4}{6}. \quad (44)$$

From the energy conservation condition $\mathcal{F}(\Delta_0; \Delta_0) = V(\Delta_0; \Delta_0) - V(0; \Delta_0) = 0$, we obtain:

$$[-1 + g^2(1 - 2\Delta_0 + 5\Delta_0^2)] \frac{\Delta_0^2}{2} + g^2 \frac{\Delta_0^4}{6} = 0. \quad (45)$$

Letting $g = 1 + \sigma$ with $\sigma \rightarrow 0^+$, and assuming a perturbative expansion:

$$\Delta_0 = A\sigma + B\sigma^2 + \mathcal{O}(\sigma^3), \quad (46)$$

we expand the left-hand side of Eq (45) in powers of σ and keep terms up to σ^2 :

$$\begin{aligned} (2\sigma + \sigma^2) - 2(1 + 2\sigma + \sigma^2)(A\sigma + B\sigma^2) \\ + \frac{16}{3}(1 + 2\sigma + \sigma^2)(A\sigma + B\sigma^2)^2 = 0, \end{aligned} \quad (47)$$

and

$$2\sigma + \sigma^2 - 2A\sigma - 2B\sigma^2 - 4A\sigma^2 + \frac{16}{3}A^2\sigma^2 = 0.$$

Matching coefficients of powers of σ , we find:

$$\begin{aligned} 2\sigma - 2A\sigma = 0 &\Rightarrow A = 1, \\ \sigma^2 - 2B\sigma^2 - 4A\sigma^2 + \frac{16}{3}A^2\sigma^2 = 0 &\Rightarrow B = \frac{7}{6}. \end{aligned} \quad (48)$$

Therefore, the solution is given by

$$\Delta_0 \sim \sigma + \frac{7}{6}\sigma^2 + \mathcal{O}(\sigma^3). \quad (49)$$

Therefore, we immediately have $-1 + g^2(1 - 2\Delta_0 + 5\Delta_0^2) \sim -\frac{1}{3}\sigma^2$. Substituting this into the expansion of $V(\Delta; \Delta_0)$, we get:

$$V(\Delta) \sim \left(\frac{1}{4}\sigma^2 + \frac{5}{6}\sigma^3 + \frac{4}{9}\sigma^4 \right) - \frac{\sigma^2}{6}\Delta^2 + (1 + 2\sigma + \sigma^2)\frac{\Delta^4}{6}, \quad (50)$$

where the first bracket indicates the constant term in the expansion obtained by inserting the expression of $\Delta_0(\sigma)$ and keeping the order up to σ^4 . Hence, the average kinetic energy is given by

$$\Gamma(\Delta) = \frac{\partial V(\Delta)}{\partial \Delta} \sim -\frac{\sigma^2}{3}\Delta + (1 + 2\sigma + \sigma^2)\frac{2\Delta^3}{3}, \quad (51)$$

which leads to Eq. (19) shown in the main text.

Algorithmic implementation of the DMFT equation

We add here the details about the implementation of the single-degree-of-freedom DMFT equations, as shown in Algorithm 1. For more implementation details of the dynamical mean-field theory, readers may refer to a pedagogical introduction [2].

Algorithm 1 DMFT Dynamics Simulation

- 1: Draw M samples of noise trajectories $\eta_t^{m,(0)}$ from a multivariate Gaussian distribution with zero mean and covariance $\langle \eta(t)\eta(t') \rangle$.
 - 2: Initialize $x^m(0) \sim \mathcal{N}(0, 1)$ for $m = 1, \dots, M$; set total time length $S = T/dt$ (dt is a small increment).
 - 3: **for** $c = 1$ to N_c **do** ▷ DMFT iteration
 - 4: **for** $t = 0$ to $S - 1$ **do**
 - 5: $x^m(t+1) \leftarrow x^m(t) + dt \cdot [-x^m(t) + \eta_t^{m,(c-1)}]$
 - 6: **end for**
 - 7: Compute $\phi^m(t) \leftarrow \tanh(x^m(t))$
 - 8: Estimate correlation: $C_{tt'} \leftarrow \frac{1}{M} \sum_{m=1}^M \phi^m(t)\phi^m(t')$
 - 9: Estimate variance: $\Delta_{tt'} \leftarrow \frac{1}{M} \sum_{m=1}^M x^m(t)x^m(t')$
 - 10: Draw $\eta_t^{m,(c)} \sim \mathcal{N}(0, g^2 C_{tt'})$ ▷ Update noise with current covariance
 - 11: **end for**
 - 12: **Output:** Final $\Delta_{tt'}$ and $C_{tt'}$
-

* Electronic address: huanghp7@mail.sysu.edu.cn

- [1] H. Sompolinsky, A. Crisanti, and H. J. Sommers. Chaos in random neural networks. *Phys. Rev. Lett.*, 61:259–262, 1988.
- [2] Wenxuan Zou and Haiping Huang. Introduction to dynamical mean-field theory of randomly connected neural networks with bidirectionally correlated couplings. *SciPost Phys. Lect. Notes*, page 79, 2024.
- [3] Junbin Qiu and Haiping Huang. An optimization-based equilibrium measure describing fixed points of non-equilibrium dy-

namics: application to the edge of chaos. *Commun. Theor. Phys.*, 77(3):035601, 2025.

- [4] Chris G. Langton. Computation at the edge of chaos: Phase transitions and emergent computation. *Physica D: Nonlinear Phenomena*, 42(1):12–37, 1990.
- [5] Nils Bertschinger and Thomas Natschlager. Real-time computation at the edge of chaos in recurrent neural networks. *Neural computation*, 16(7):1413–1436, 2004.
- [6] Dean V. Buonomano and Wolfgang Maass. State-dependent computations: spatiotemporal processing in cortical networks. *Nature Reviews Neuroscience*, 10(2):113–125, 2009.
- [7] David Sussillo and Larry F Abbott. Generating coherent patterns of activity from chaotic neural networks. *Neuron*, 63(4):544–557, 2009.
- [8] Saurabh Vyas, Matthew D. Golub, David Sussillo, and Krishna V. Shenoy. Computation through neural population dynamics. *Annual Review of Neuroscience*, 43:249–275, 2020.
- [9] Haiping Huang. Eight challenges in developing theory of intelligence. *Front. Comput. Neurosci.*, 18:1388166, 2024.
- [10] Srdjan Ostojic and Stefano Fusi. Computational role of structure in neural activity and connectivity. *Trends in Cognitive Sciences*, 28(7):677–690, 2024.
- [11] Jakob Stubenrauch, Christian Keup, Anno C. Kurth, Moritz Helias, and Alexander van Meegen. Fixed point geometry in chaotic neural networks. *Phys. Rev. Res.*, 7:023203, 2025.
- [12] Weizhong Huang and Haiping Huang. Freezing chaos without synaptic plasticity. *arXiv:2503.08069*, 2025.
- [13] Shishe Wang and Haiping Huang. How high dimensional neural dynamics are confined in phase space. *arXiv:2410.19348*, 2024.
- [14] Samantha J. Fournier, Alessandro Pocco, Valentina Ros, and Pierfrancesco Urbani. Non-reciprocal interactions and high-dimensional chaos: comparing dynamics and statistics of equilibria in a solvable model. *arXiv:2503.20908*, 2025.
- [15] David Sussillo and Omri Barak. Opening the black box: Low-dimensional dynamics in high-dimensional recurrent neural networks. *Neural Computation*, 25:626–649, 2013.
- [16] A. Crisanti and H. Sompolinsky. Path integral approach to random neural networks. *Phys. Rev. E*, 98:062120, 2018.
- [17] Haiping Huang. *Statistical Mechanics of Neural Networks*. Springer, Singapore, 2022.
- [18] Francesco Ferraro, Christian Grilletta, Amos Maritan, Samir Suweis, and Sandro Azaele. Exact solution of dynamical mean-field theory for a linear system with annealed disorder. *Journal of Statistical Mechanics: Theory and Experiment*, 2025(2):023301, 2025.
- [19] Rishidev Chaudhuri, Berk Gerçek, Biraj Pandey, Adrien Peyrache, and Ila Fiete. The intrinsic attractor manifold and population dynamics of a canonical cognitive circuit across waking and sleep. *Nature Neuroscience*, 22(9):1512–1520, 2019.
- [20] Ramon Nogueira, Chris C. Rodgers, Randy M. Bruno, and Stefano Fusi. The geometry of cortical representations of touch in rodents. *Nature Neuroscience*, 26(2):239–250, 2023.
- [21] Li-Ru Zhang. <https://github.com/.....>, 2025.